



Nanodiamond decorated 2D hexagonal Fe₂O₃ nanosheets with a Z-scheme photogenerated electron transfer path for enhanced photocatalytic activity

Jingjing Pan¹, Feng Guo^{1,*}, Haoran Sun¹, Mingyang Li¹, Xiufeng Zhu¹, Lingling Gao¹, and Weilong Shi^{2,*} 

¹ School of Energy and Power, Jiangsu University of Science and Technology, Zhenjiang 212003, Jiangsu, People's Republic of China

² School of Material Science and Engineering, Jiangsu University of Science and Technology, Zhenjiang 212003, People's Republic of China

Received: 20 August 2020

Accepted: 14 December 2020

Published online:

3 January 2021

© The Author(s), under exclusive licence to Springer Science+Business Media, LLC part of Springer Nature 2021

ABSTRACT

Herein, a unique 0D/2D nanodiamonds (NDs)/hematite (Fe₂O₃) composite photocatalyst was constructed by the solvothermal method and then was used to remove tetracycline pollutants in the aqueous solution, where the NDs nanoparticles were tightly anchored on the surface of hexagonal Fe₂O₃ nanosheets. The superior photocatalytic performance (85%, 180 min) was obtained by the optimum 15-NDs/Fe₂O₃ composite sample (containing 15 wt% NDs), which is approximately 4.13 times higher than that of pure Fe₂O₃. This is because the introduction of NDs nanoparticles not only promotes the visible-light absorption of Fe₂O₃, but also facilitates the separation of photogenerated electrons and holes in the interface of composite by the design of Z-scheme heterostructure. Besides, the intermediates, active species and reaction mechanism in the photocatalytic process were also discussed. This work enriches the knowledge in designing of novel 0D/2D Z-scheme heterojunction composites for photocatalysis.

Introduction

Collection and conversion of solar energy into active radicals through photocatalytic oxidation technology are considered as a potential and promising approach to address the environmental pollution [1–7]. In the past decades, extensive efforts have been made for

developing high-efficient visible light-responsive photocatalysts for the degradation of organic contaminants in wastewater [8–11]. Hematite (Fe₂O₃), composed of naturally abundant Fe and O elements, is an attractive photocatalyst mainly due to its inherent narrow band gap (2.0–2.2 eV), which enables a wide range of solar light utilization to reach 600 nm [12–16]. The other advantages of

Handling Editor: Dale Huber.

Address correspondence to E-mail: gfeng0105@126.com; shiwl@just.edu.cn

<https://doi.org/10.1007/s10853-020-05700-5>

environmental friendliness, low cost and excellent chemical stability further make it possess great potential application in the field of photocatalysis [17, 18]. Frustratingly, the photocatalytic performance of Fe_2O_3 is still much lower than the expected because of the sluggish charge transfer kinetics, poor electron–hole pairs separation and limited specific surface area [19–21], which is a very urgent problem to be solved. In recent years, fabricating heterojunctions with other semiconductors have been reported as an effective strategy to achieve high catalytic activity, especially to form the Z-scheme heterojunction [22, 23]. This is because the Z-scheme heterojunction can exhibit a more admirable advantage in electron-hole pair separation, while the strong redox ability of the composite photocatalyst can be maintained since the reduction and oxidation reactions occur on the semiconductors with higher reduction and oxidation potentials, respectively [24]. For example, the Z-scheme heterojunction composites of $\text{Fe}_2\text{O}_3/\text{g-C}_3\text{N}_4$ [25], $\text{BiVO}_4 @\text{Fe}_2\text{O}_3$ [26], $\text{Sb}_2\text{Se}_3/\text{Fe}_2\text{O}_3$ [27], $\text{Fe}_2\text{O}_3/\text{CuBi}_2\text{O}_4$ [28] and so on. In this regard, the development and design of efficient Fe_2O_3 -based Z-scheme heterojunction photocatalyst are highly desired.

In addition to designing electron transfer paths through the formation of heterojunctions, the interfacial contact of composites is also a key factor for affecting photocatalytic activity of semiconductor photocatalyst. Recently, the rational design of constructing zero dimension/two dimension (0D/2D) heterojunction has gained more noticed due to the following merits: (i) 0D/2D heterojunction often exhibits larger interface contact area for providing more reactive sites; and (ii) the close interactions between 0 and 2D materials can not only make 0D material more dispersive and stable, but also facilitate the photo-induced charge transfer of 2D material [23, 29–31]. Hence, the fast separation and transfer of photogenerated carriers can be expected to achieve in 0D/2D Z-scheme heterojunction photocatalysts.

Nanodiamonds (NDs), as a novel 0D carbon nanomaterial, possess the special crystalline structure with sp^3 -hybridized C atoms and small Bohr radius in comparison with traditional nanocarbon materials, thus having unique photoelectric properties, such as unrivalled carrier mobility and large exciton binding energy [32–34]. It is worth mentioning that the excellent chemical stability, thermal conductivity, photobleaching resistance and the lowest toxicity

among various carbon materials of NDs not only ensure its excellent corrosion resistance during the photocatalytic process, but also make it satisfy more sustainable in the view of practical applications [35, 36]. Up to now, the synthesis and photocatalytic activity of 0D/2D NDs/ Fe_2O_3 heterojunction photocatalyst have not been reported.

In this work, the 0D/2D NDs/ Fe_2O_3 Z-scheme heterostructure was constructed by a facile one-step solvothermal method for degradation of tetracycline (TC) under visible light irradiation. The result demonstrated that the fabrication of heterojunction between 0D NDs and 2D hexagonal Fe_2O_3 nanosheets could effectively hamper the photogenerated carriers recombination, which greatly improve the photocatalytic performance. Finally, the Z-scheme photogenerated electron transfer path mechanism of 0D/2D NDs/ Fe_2O_3 composite photocatalyst was proposed in detail.

Experimental

Materials

NDs with an average size of 5–10 nm were purchased from XFNANO Science and Technology Ltd. (Nanjing, China). $\text{FeCl}_3 \cdot 6\text{H}_2\text{O}$, CH_3COONa and ethanol were purchased from Sinopharm Chemical Reagents Co., Ltd (Shanghai, China) and were of analytical reagent grade.

Synthesis of NDs/ Fe_2O_3 photocatalysts

The NDs decorated Fe_2O_3 hexagonal nanosheets (NDs/ Fe_2O_3) composite photocatalysts were synthesized via a one-step simple solvothermal process. Firstly, 1.092 g $\text{FeCl}_3 \cdot 6\text{H}_2\text{O}$ was dispersed in the mixture of 40 mL ethanol and 2.8 mL H_2O . Then, 3.2 g CH_3COONa was added to the above solution and stirred for 30 min. Subsequently, a certain mass fraction of NDs powder with weight ratios of 5, 10, 15, 20 and 25% in the NDs/ Fe_2O_3 composites was introduced and mixed uniformly. Next, the homogeneous solution was transferred into a Teflon-lined stainless steel vessel with a capacity of 100 mL and heated at 180 °C for 12 h. After that, the precipitants were collected and rinsed with distilled water and ethanol several times. Finally, the NDs/ Fe_2O_3 can be obtained after dried in the oven at 6 °C for 10 h. The

obtained samples were labeled as x -NDs/ Fe_2O_3 ($x = 5, 10, 15, 20$ and 25). The preparation process of pure Fe_2O_3 hexagonal nanosheets is similar to NDs/ Fe_2O_3 without adding NDs powder. The synthetic processes of Fe_2O_3 and NDs/ Fe_2O_3 are schematically illustrated in Scheme 1.

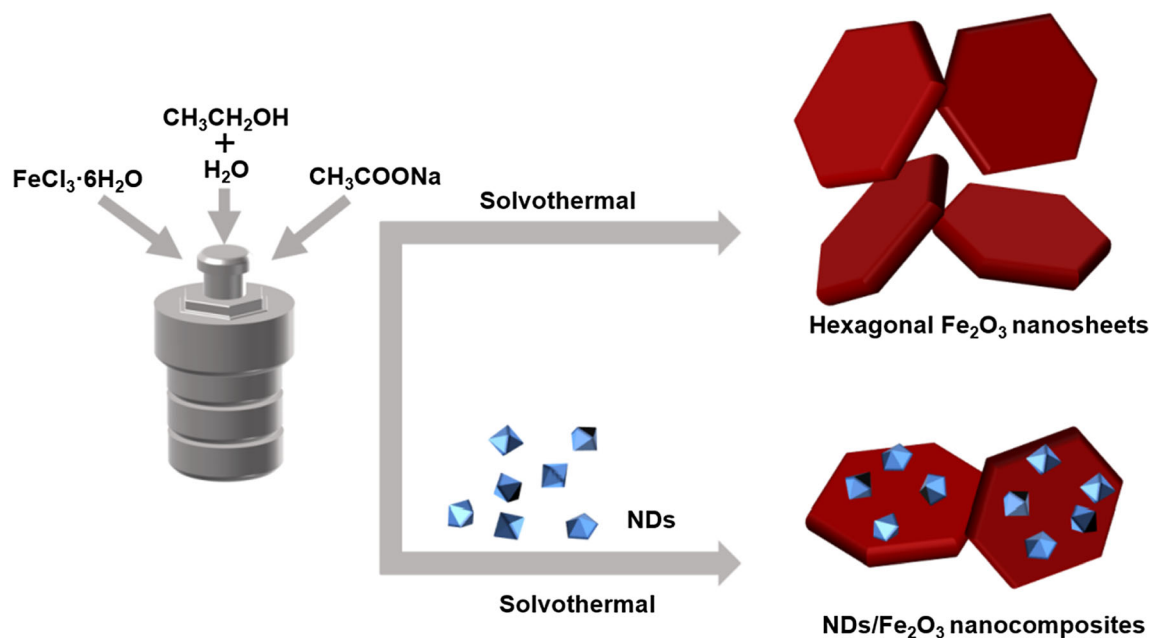
Photocatalytic reaction

The photocatalytic performance of as-prepared samples was estimated for photodegradation of tetracycline (TC) under visible light irradiation ($\lambda > 420$ nm). Typically, 50 mg catalyst was dispersed in 100 mL of 10 mg/L TC aqueous solution. The suspensions were stirred for 30 min in the dark to get the adsorption–desorption equilibrium prior to light irradiation. After that, the suspensions were illuminated by a 300 W Xe lamp (CEL-HXF300-T3, Beijing Zhongjiao Jinyuan Technology Co., Ltd.) with a 420 nm cut-off filter. Subsequently, 3.5 mL solution was extracted and centrifuged to remove the samples every certain time intervals. The TC concentrations at different time intervals were calculated by measuring the absorbance of the supernatant at 357 nm with UV–vis spectrophotometer (UV-2450). The characterizations, active species capturing and electronic spin resonance (ESR) tests can be gained in the **Supporting Information**.

Results and discussion

The crystallographic structure and phase composition of Fe_2O_3 , NDs and a series of NDs/ Fe_2O_3 nanocomposites were examined by X-ray diffraction (XRD) analysis and displayed in Fig. 1. For pure Fe_2O_3 , the strong diffraction peaks at $2\theta = 24.2^\circ, 33.3^\circ, 35.6^\circ, 41.1^\circ, 49.6^\circ, 54.1^\circ, 57.5^\circ, 62.2^\circ$ and 64.1° are corresponding to (012), (104), (110), (113), (024), (116), (018), (214) and (300) crystal planes of Fe_2O_3 (JCPDS No. 33–0664), respectively [37]. And the NDs exhibit the diffraction peaks at $2\theta = 43.9^\circ$ and 75.4° , which are ascribed to (111) and (220) crystal planes of diamond, respectively [33]. As for NDs/ Fe_2O_3 nanocomposites with different amounts of NDs, no peak position shift was observed, which indicated that the NDs nanoparticles were stacked on the outer surface of Fe_2O_3 . Furthermore, although the peaks of NDs are very weak in NDs/ Fe_2O_3 composites, the existence of NDs also can be described by the enhanced peak intensity of (111) crystal planes in NDs/ Fe_2O_3 nanocomposites. Based on the above results, NDs/ Fe_2O_3 composites were successfully prepared by the facile solvothermal method.

The morphologies of the prepared samples were characterized by scanning electron microscope (SEM). In Fig. 2a, the Fe_2O_3 exhibits a uniform hexagonal nanosheet structure with the diameter size of ~ 100 nm and thickness size of ~ 20 nm. The



Scheme 1 Illustration for preparation of hexagonal Fe_2O_3 nanosheets and NDs/ Fe_2O_3 nanocomposites.

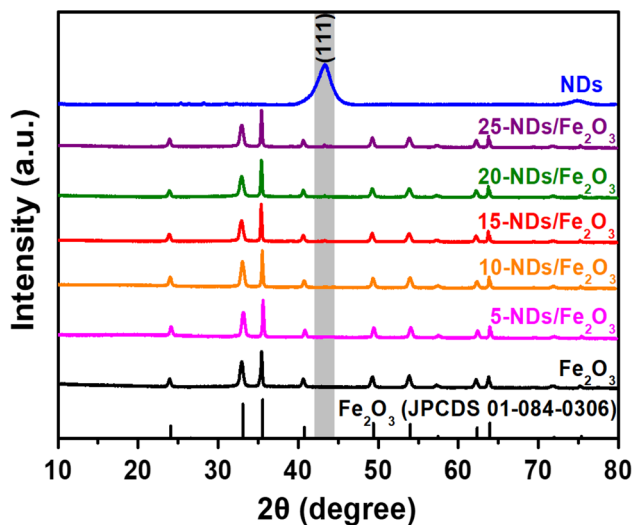


Figure 1 XRD patterns of Fe_2O_3 and $\text{NDs}/\text{Fe}_2\text{O}_3$ nanocomposites.

morphology of 15-NDs/ Fe_2O_3 still remains hexagonal nanosheets compared to the pristine Fe_2O_3 . Meanwhile, it is difficult to observe and confirm whether the NDs exists in the composite, which may be due to the small size of the NDs. Further analysis and observation of nanocomposites through transmission electron microscopy (TEM) techniques are therefore required. In addition, through the contrast of X-ray energy disperse spectroscopy (EDS) patterns (insets of Fig. 2a and b), it can be clear that the content of C in the 15-NDs/ Fe_2O_3 composite has been increased obviously, indicating that there is a combination of carbon substances and Fe_2O_3 .

To more clearly disclose the morphologies and microstructures of $\text{NDs}/\text{Fe}_2\text{O}_3$, TEM images were

investigated. From Fig. 3a and b, it can be seen that the NDs with average diameter of ~ 5 nm are loaded on the Fe_2O_3 hexagonal nanosheets to form 0D/2D heterostructure. From the HRTEM image in Fig. 3c, the lattice spacing is calculated to be 0.25 and 0.21 nm, which corresponded to the (110) and (111) crystallographic planes of Fe_2O_3 and NDs, respectively [32, 38]. Furthermore, the elemental mapping images (Fig. 3d) of $\text{NDs}/\text{Fe}_2\text{O}_3$ reveal the presence of Fe, O and C in the selected area, verifying the successful preparation of $\text{NDs}/\text{Fe}_2\text{O}_3$ nanocomposite.

For studying the optical absorption properties of the as-prepared photocatalysts, the UV–vis absorption spectra were performed. From Fig. 4a, the absorption band edges of Fe_2O_3 and NDs are approximately located at 620 nm and 580 nm, respectively, which are in agreement with previous reports [33, 38]. Compared with pure Fe_2O_3 , the enhanced visible light absorption for 15-NDs/ Fe_2O_3 can be observed, demonstrating the sensitization effect is obtained due to the introduction of NDs in the composite. As plotted in Fig. 4b, according to the Kubelka–Munk function [28], the band gaps (E_g) of Fe_2O_3 and NDs were estimated to be 1.98 V and 2.15 eV, respectively. Next, the valence band (E_{VB})-XPS spectra were employed to determine the VB positions of Fe_2O_3 and NDs. From Fig. 4c, the VB positions of Fe_2O_3 and NDs were measured to be 2.51 eV and 1.54 eV, respectively. By the conversion of the following formula (1):

$$E_{\text{NHE}}/\text{V} = \Phi + E_{\text{VL}}/\text{eV} - 4.44 \quad (1)$$

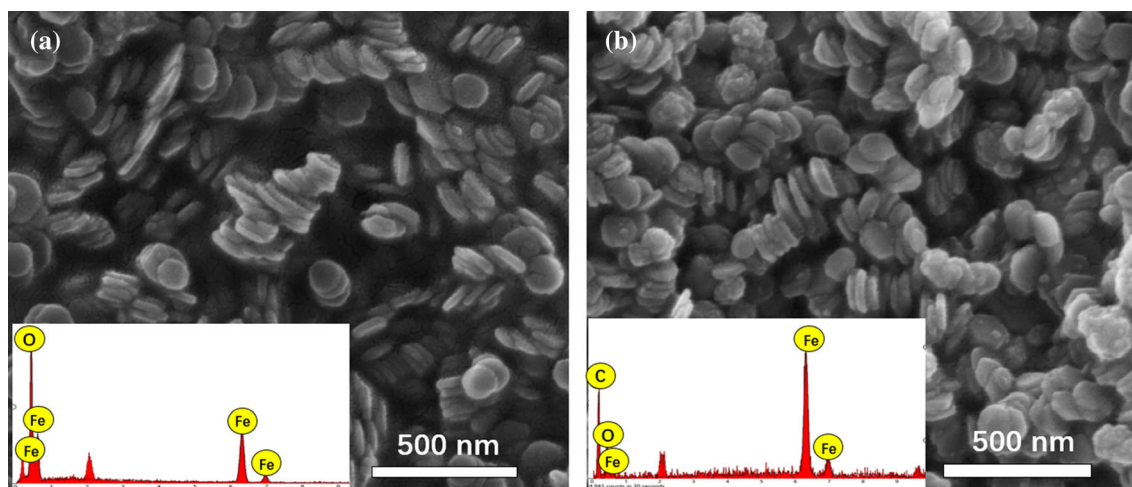
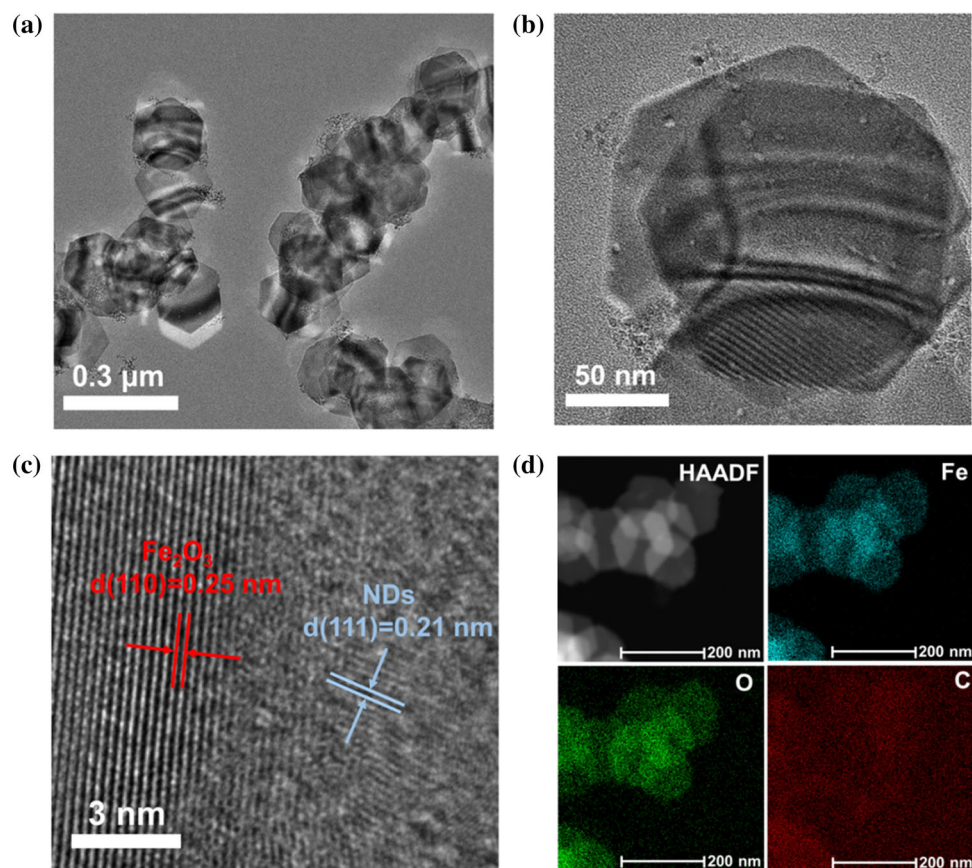


Figure 2 SEM images and measured EDS spectra (insets) of **a** Fe_2O_3 and **b** 15-NDs/ Fe_2O_3 .

Figure 3 a, b TEM, c HRTEM and d HAADF-SEM and the corresponding elemental mapping images of 15-NDs/Fe₂O₃.



where the E_{NHE} , Φ and E_{VL} are on behalf of potential of normal hydrogen electrode (NHE), the analyzer electron work function (4.30 eV) and the vacuum level (VL) potential, respectively [39]. The VB positions of Fe₂O₃ and NDs are 2.37 V and 1.4 V vs. NHE, respectively. Based on the band gaps following formula (2): $E_g = E_{\text{VB}} - E_{\text{CB}}$ [39], the CB positions and the band energy alignments of Fe₂O₃ and NDs are given in Fig. 4d.

The surface chemical compositions of as-prepared products were measured by the X-ray photoelectron spectroscopy (XPS). All the XPS spectra were calibrated by the standard peak of C 1s located at 284.8 eV and Fe and O elements in both Fe₂O₃ and NDs/Fe₂O₃ can be seen from the survey spectra displayed in Fig.S1. Obviously, it can be observed that the C peak intensity of 15-NDs/Fe₂O₃ is higher than that of Fe₂O₃, which explains the introduction of additional C in composite. From Fig. 5a, the Fe 2p spectrum of pristine Fe₂O₃ centered at binding energies of 710.4 eV and 723.7 eV is corresponding to Fe 2p_{3/2} and Fe 2p_{1/2}, respectively [38], while the satellite peaks at 718.2 eV and 732.5 eV are the typical

value of Fe³⁺ in the sample [40]. In Fig. 5b, the O 1s spectra core level for Fe₂O₃ and 15-NDs/Fe₂O₃ were slightly different. The Fe₂O₃ exhibits two peaks located at 529.5 eV and 531.0 eV in the O 1s spectrum, which belong to the Fe–O bond and –OH groups, respectively [41], while the 15-NDs/Fe₂O₃ composite shows three peaks centered at 529.3, 530.9 and 532.8 eV that could be ascribed to the presences of Fe–O and –OH and carbon phase (C–O) bonds, respectively [42]. The above results demonstrate the strong interaction between NDs and Fe₂O₃, resulting in the effective charge migration in the composite photocatalyst during the photocatalysis.

The degradation experiments of TC were carried out under visible light to evaluate the photocatalytic performance of as-prepared photocatalysts. Before the photodegradation, the reaction solution was placed in the dark and stirred for 30 min to reach adsorption equilibrium. From the adsorption curves displayed in Fig. 6a, all samples reached adsorption equilibrium within 30 min dark reaction and with the increase of NDs content, the adsorption properties of the synthesized materials gradually increased. As

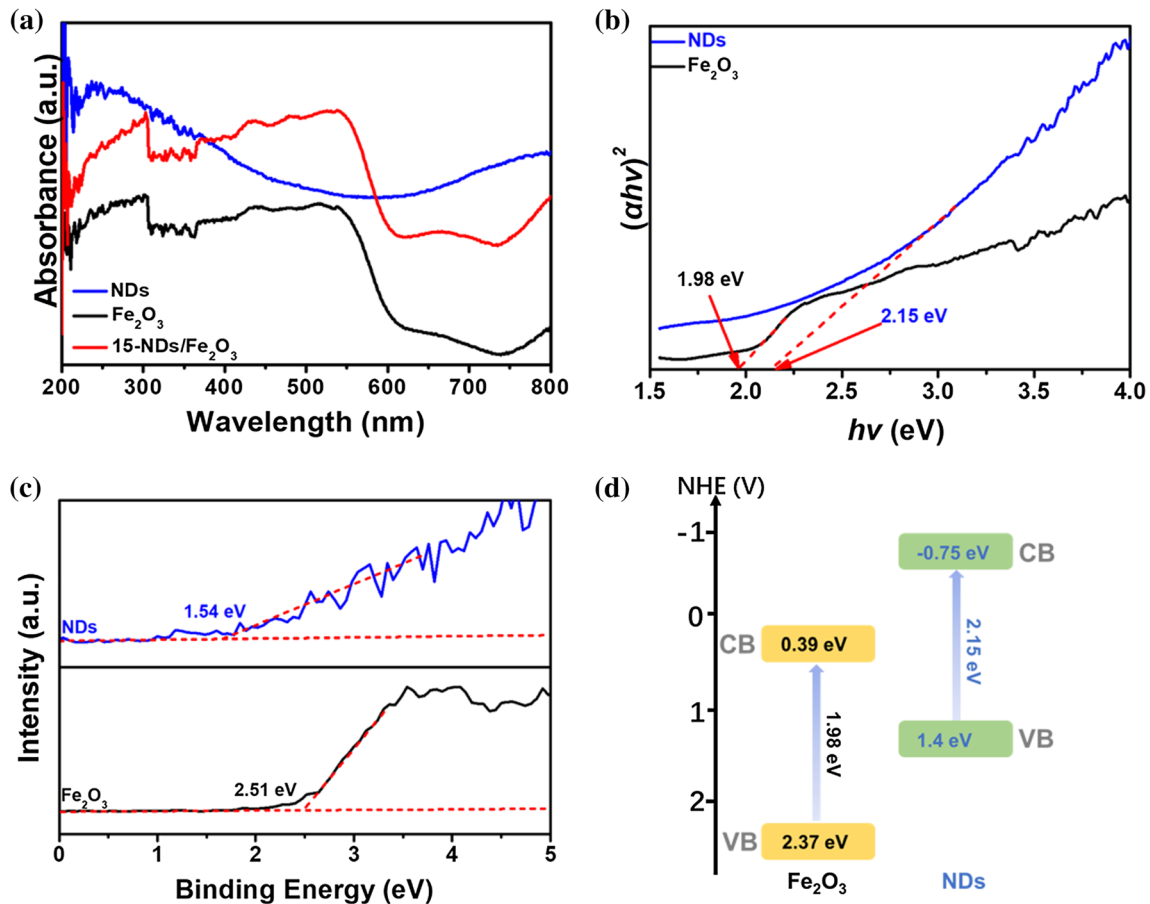


Figure 4 a UV-vis absorption spectra of NDs, Fe₂O₃ and 15-NDs/Fe₂O₃. b E_g values for NDs and Fe₂O₃. c Valence band XPS measurements for NDs and Fe₂O₃. d Band structure diagrams of NDs and Fe₂O₃.

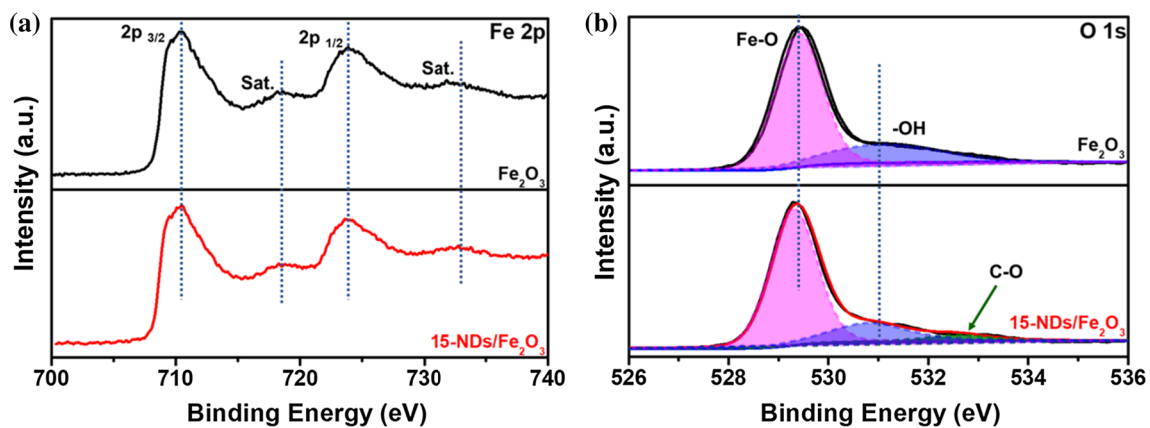


Figure 5 High-resolution XPS spectra of the a Fe 2p and b O 1s of Fe₂O₃ and 15-NDs/Fe₂O₃.

exhibited in Fig. 6b, for the blank test, less than 0.2% of TC was decomposed after 3 h under visible light irradiation, demonstrating the self-degradation by photosensitization of TC can be negligible. Pure Fe₂O₃ exhibited a poor degradation efficiency of TC

was around 20.6% in 3 h. Significantly, when Fe₂O₃ is coupled with NDs, the photocatalytic activity has been enhanced, which can be ascribed to the improved adsorption of organic pollutants and transfer of photogenerated electrons of composite.

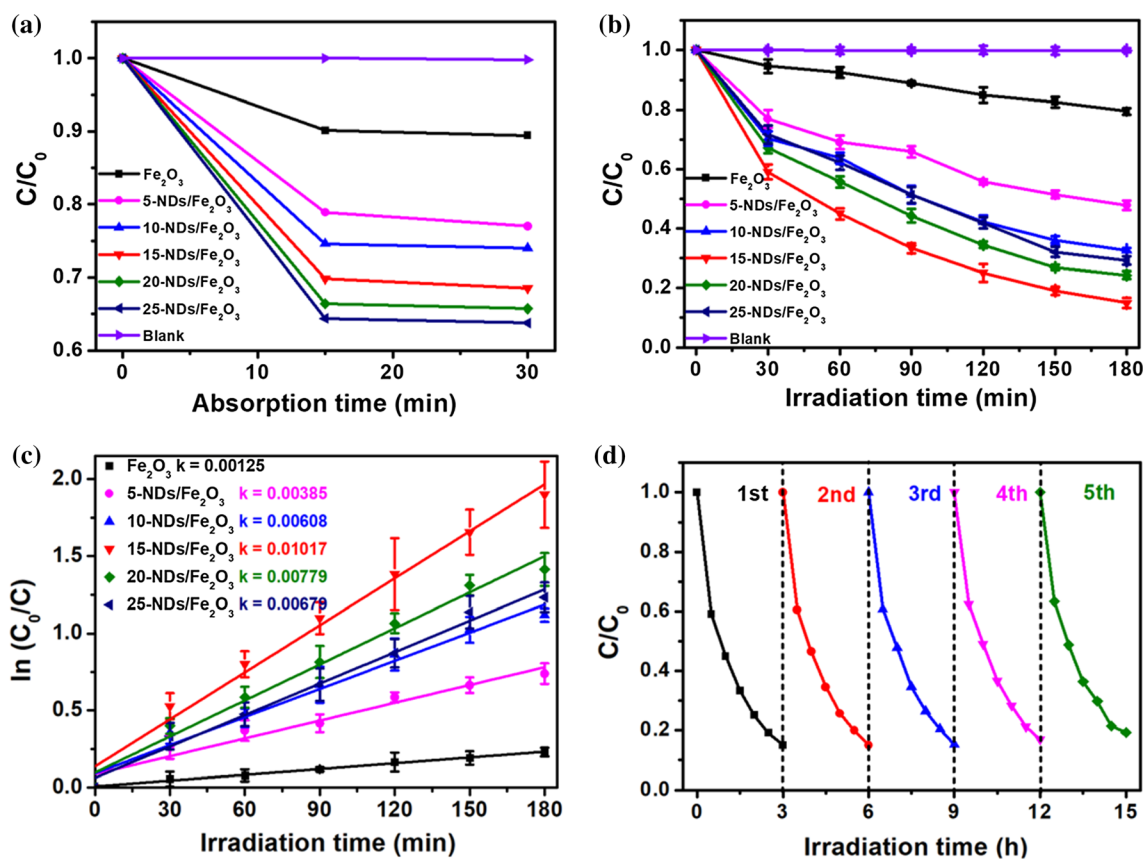


Figure 6 **a** Absorption properties of TC over as-synthesized samples and blank test for TC degradation. **b** Photodegradations of TC over as-prepared products under visible irradiation ($\lambda > 420$ nm). **c** First-order kinetics and corresponding rate

constants of TC degradation curves over different samples. **d** Cycling runs for the photocatalytic TC degradation in the presence of 15-NDs/ Fe_2O_3 sample.

The 15-NDs/ Fe_2O_3 sample achieved the optimum photocatalytic activity with best degradation TC rate of 85%, which is about 4.12 times higher than that of pristine Fe_2O_3 . As the further increase content of NDs (more than 15 wt.%) in composite, the photocatalytic performance presents a downward trend. This decreased photocatalytic activity could be ascribed to the agglomeration of the excessive NDs, which hampered the interfacial charge separation [33]. Moreover, the active sites could be blocked and the effective contact could be reduced because of too intensive decoration of NDs. To further compare the photocatalytic activity of as-prepared samples, the rate constant k values of TC degradation were calculated based on the pseudo-first-order kinetic plots and displayed in Fig. 6c. Obviously, the rate constant k of 15-NDs/ Fe_2O_3 reaches to 0.01017 min^{-1} , which is 8.136 times higher than that of pure Fe_2O_3 (0.00125 min^{-1}). Additionally, the photocatalytic parameters of the NDs/ Fe_2O_3 sample for TC

degradation were further compared with the previous reports. As detail listed in Table S1, the 15-NDs/ Fe_2O_3 sample indeed exhibits excellent visible light-driven photocatalytic activity for TC degradation. Therefore, the results demonstrate that the NDs/ Fe_2O_3 Z-scheme heterojunction photocatalyst can be used as a promising photocatalyst for removal of antibiotic contaminants. For determining the practical application potential of as-prepared 15-NDs/ Fe_2O_3 composite, its stability was tested by cycling experiments. As prepared in Fig. 6d, more than 80% of TC can be degraded after five runs, proving the tight bond between 0D NDs and 2D Fe_2O_3 by the solvothermal reaction process, demonstrating that as-prepared NDs/ Fe_2O_3 possesses excellent reusability and stability.

To gain more information on the specific surface area, nitrogen adsorption–desorption isotherms of Fe_2O_3 and NDs/ Fe_2O_3 were determined. From Fig. 7a, both Fe_2O_3 and NDs/ Fe_2O_3 possess type IV

isotherms, indicating the mesoporous nature of as-synthesized photocatalysts [43, 44]. And the decoration of NDs on hexagonal Fe_2O_3 nanosheets will give rise to an enhance of the specific surface area ($56.61 \text{ m}^2\text{g}^{-1}$) in comparison with that of pure Fe_2O_3 ($19.96 \text{ m}^2\text{g}^{-1}$), which can provide more reactive sites for adsorption and photocatalysis. To reveal the correlation between photocatalytic performance and photo-induced carriers separation of the photocatalysts, photoluminescence (PL) spectra were conducted for Fe_2O_3 and 15-NDs/ Fe_2O_3 samples. From Fig. 7b, the PL spectra of the prepared samples were excited with the wavelength of 360 nm and the emission intensity of 15-NDs/ Fe_2O_3 is obviously weakened compared with the pure Fe_2O_3 , indicating that the recombination rate of photogenerated electron–hole pairs in the NDs/ Fe_2O_3 nanocomposite is low, which is agreement with previous reports [45–47]. Photoelectrochemical measurements were performed to further investigate the charge transfer ability of as-prepared products. As shown in Fig. 7c,

the transient photocurrent response intensity of 15-NDs/ Fe_2O_3 was much higher than that of pristine Fe_2O_3 , demonstrating the higher mobility of photo-generated charges [48, 49]. The consistent change can be also observed in electrochemical impedance spectroscopy (EIS) plots (Fig. 7d), the much smaller radius can be found for 15-NDs/ Fe_2O_3 , which implies the effective charge migration in the nanocomposite [50–52]. Based on the above analysis, there is no doubt that the recombination of the carriers can be significantly hampered by the heterojunction, which plays an important role in enhancing photocatalytic activity.

Active species capture experiments were performed to investigate the active species of NDs/ Fe_2O_3 for the photocatalytic degradation of TC. The trapping quenchers, such as isopropanol (IPA), ethylenediaminetetraacetic acid disodium (EDTA-2Na) and p-benzoquinone (BQ), were used to capture the hydroxyl radicals ($\bullet\text{OH}$), holes (h^+) and superoxide radicals ($\bullet\text{O}_2^-$), respectively. As shown in

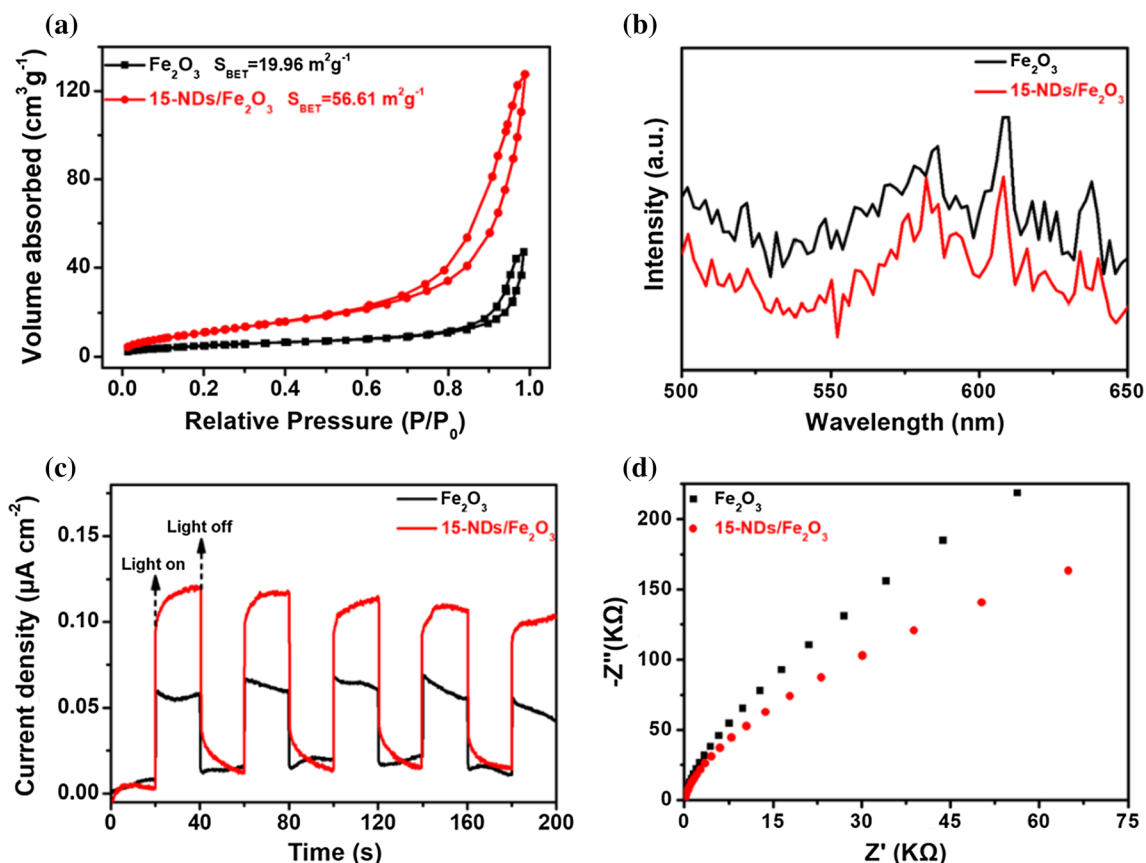


Figure 7 **a** Nitrogen adsorption–desorption isotherm curves, **b** PL spectra, **c** photocurrent response density and **d** EIS spectra of Fe_2O_3 and 15-NDs/ Fe_2O_3 composite.

Fig. 8a, photocatalysis degradation of TC decreased with the introduction EDTA-2Na and BQ, while IPA shows little effect on the TC degradation, indicating that h^+ and $\bullet\text{O}_2^-$ participated in the system as the main active species. To further verify the charge carrier migration in the photocatalytic system over NDs/ Fe_2O_3 , the ESR spin-trap technology was also carried out. The ESR signals of as-prepared samples under visible light irradiation and in the dark are presented in Fig. 8b. No peaks are observed in the dark or under visible light irradiation for the Fe_2O_3 sample, revealing that it cannot produce $\bullet\text{O}_2^-$ due to its relatively positive conduction band position of Fe_2O_3 . For the 15-NDs/ Fe_2O_3 composite, it exhibited strong DMPO- $\bullet\text{O}_2^-$ signal intensities under visible light irradiation. Thus, $\bullet\text{O}_2^-$ was produced during the photocatalysis, confirming that the photo-induced charge carriers migration pathway could follow the Z-scheme approach instead of the type II heterojunction approach.

The Z-Scheme type photogenerated charge migration in NDs/ Fe_2O_3 was proposed and illustrated in Fig. 9. Under the visible light excitation, the photogenerated electrons are produced and transferred from VB to CB of Fe_2O_3 , leaving the holes in the VB, while the same process occurred simultaneously in the NDs. The electrons in the CB of Fe_2O_3 are more liable transferred to the VB of NDs and combined with the holes in the VB of NDs through follow the Z-scheme type photogenerated charge migration pathway. Consequently, the recombination of photogenerated carriers in NDs/ Fe_2O_3 can be effectively suppressed. Because of the more negative CB edge potential of NDs than that of $\text{O}_2/\bullet\text{O}_2^-$ (-0.33 V/

NHE) [53], the photogenerated electrons in the CB of NDs can be trapped by the absorbed oxygen molecules to produce $\bullet\text{O}_2^-$ for degradation process of TC. Meanwhile, the holes on the VB of Fe_2O_3 can directly oxidize the TC to its corresponding small molecule degraded products. In addition, the 2D nanosheet structure of Fe_2O_3 allows more evenly distribution of 0D NDs nanoparticles, thus providing more active sites for photocatalysis. In this regard, the advantageous combination of 0D/2D structure and Z-scheme system can effectively improve the efficient treatment of organic pollutants.

The degradation intermediates were determined using liquid chromatography–mass spectrometry (LC–MS), and the obtained MS spectra after photocatalysis over NDs/ Fe_2O_3 are displayed in Fig.S2. According to these intermediates, the possible pathways of TC direct photocatalysis were proposed and illustrated in Fig. 10. For Pathway I, the formation of Product 1 ($m/z = 400$) was proposed to form via loss of N-methyl groups and hydroxyl group. Then, Product 1 ($m/z = 400$) was further degraded to the generation of Product 2 ($m/z = 279$) through deamination and ring-opening reaction. Afterward, Product 2 ($m/z = 279$) might undergo dehydroxylation and cleavage of carboatomic ring to yield Product 3 ($m/z = 125$) [54]. For Pathway II, Product 4 ($m/z = 416$) was stemmed from TC degradation via detachments of N-methyl and amino group. And the Product 4 ($m/z = 416$) can further transform to Product 5 ($m/z = 398$) by dehydration reaction [55]. For Pathway III, the degradation first happens via add hydrogen to the carbonyl due to its instability and went through the dislodge of N-methyl group, the Product 6 ($m/$

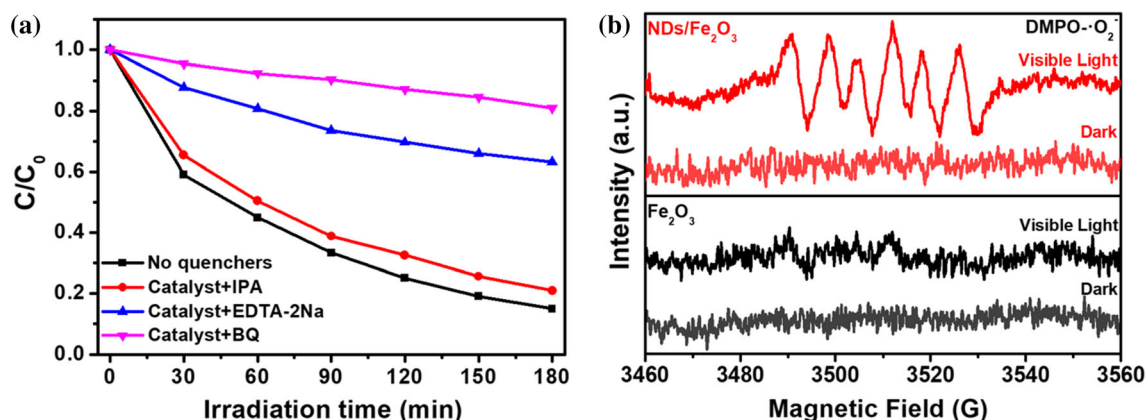


Figure 8 a Effect of different quenchers on the degradation of TC by the 15-NDs/ Fe_2O_3 . b ESR spectra of DMPO- O_2^- for Fe_2O_3 and the 15-NDs/ Fe_2O_3 nanocomposite in dark and visible light irradiation.

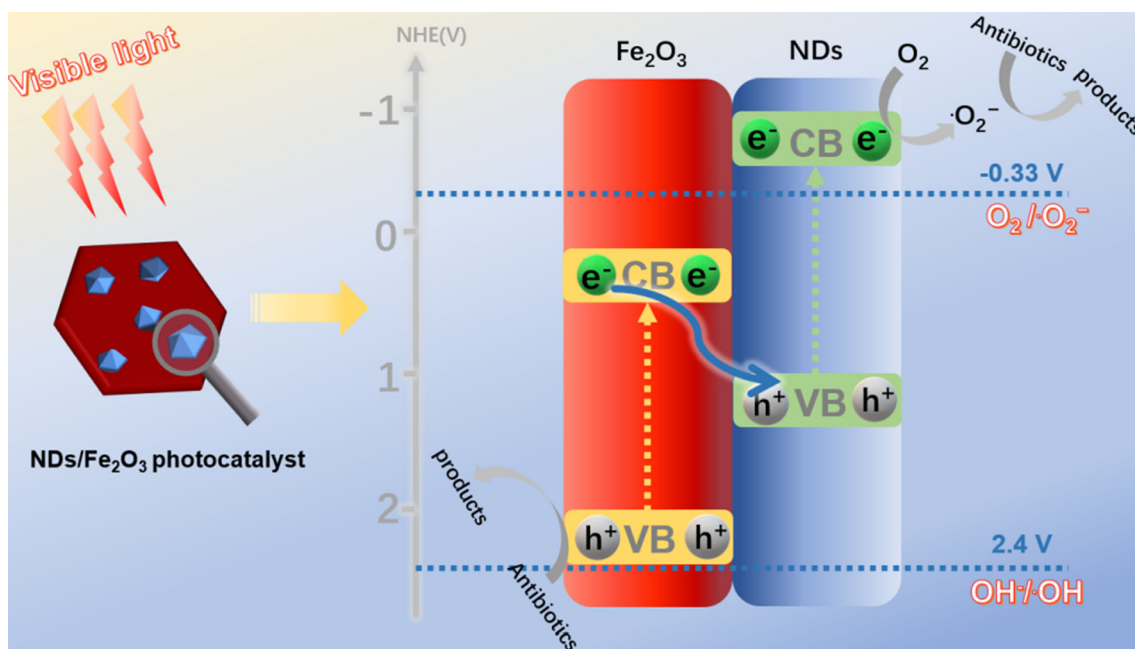


Figure 9 Possible photocatalytic mechanism and schematic structure for NDs/Fe₂O₃ nanocomposite photocatalyst.

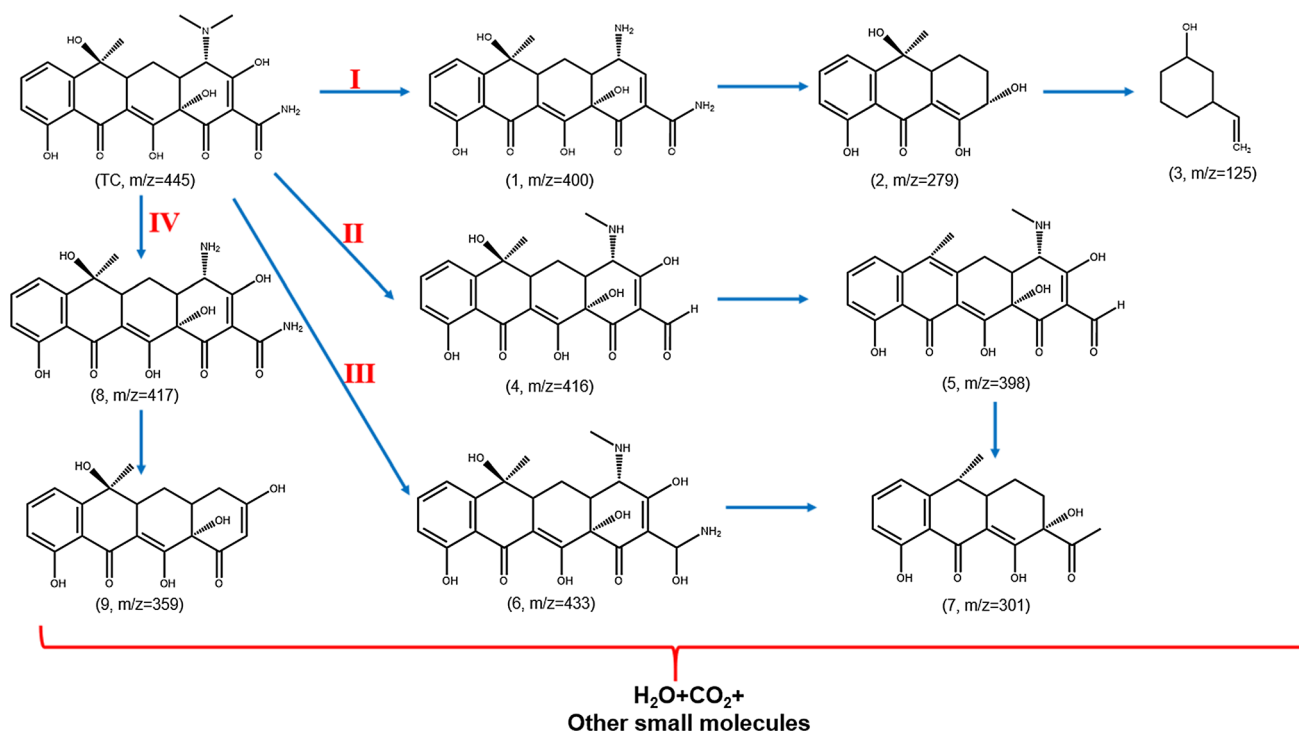


Fig. 10 Proposed transformation pathways and intermediates of TC degradation over as-prepared NDs/Fe₂O₃ composite photocatalyst.

$z = 433$) was formed. Both 5 ($m/z = 398$) and Product 6 ($m/z = 433$) can undergo carboatomic ring breakage and dehydroxylation reaction transferred into Product 7 ($m/z = 301$) [56]. For Pathway IV, the generation of Product 8 ($m/z = 417$) was attributed to the

loss of the N-methyl. Subsequently, Product 8 ($m/z = 417$) may be fragmented into Product 9 ($m/z = 359$) by loss the-CONH₂ and amino group [57]. Finally, all polar intermediates would be degraded in

to H₂O, CO₂ and other non-toxic small molecules during the photocatalysis.

Conclusion

In conclusion, a novel 0D/2D Z-scheme heterojunction of NDs/Fe₂O₃ photocatalyst was successfully fabricated by a facial one-step solvothermal process. Benefiting from the intimate contact between 0D NDs nanoparticles and 2D hexagonal Fe₂O₃ nanosheets, the NDs/Fe₂O₃ composites exhibit enhanced photocatalytic performance compared to pristine Fe₂O₃. These enhancements can be attributed to the effective Z-scheme charge transfer pathway between the heterojunction interface, thus facilitating the photoexcited e⁻-h⁺ separation and remaining the superior redox capability of the photocatalyst. In addition, the decoration of NDs on Fe₂O₃ nanosheet can give rise to an improvement of the specific surface area, which could provide more reactive sites for photocatalysis. This work sets a preminent example of the fabrication of efficacious photocatalyst for photocatalytic degradation of organic contaminants.

Acknowledgements

National Natural Science Foundations of China (Nos. 21906072 and 22006057), the Natural Science Foundation of Jiangsu Province (BK20190982), Doctoral Scientific Research Foundation of Jiangsu University of Science and Technology (China) (1062931806 and 1142931803) and “Doctor of Mass entrepreneurship and innovation” Project in Jiangsu Province.

Supplementary Information: The online version contains supplementary material available at (<http://doi.org/10.1007/s10853-020-05700-5>).

References

- [1] Zhang G, Chen D, Li N, Xu Q, Li H, He J, Lu J (2019) Fabrication of Bi₂MoO₆/ZnO hierarchical heterostructures with enhanced visible-light photocatalytic activity. *Appl Catal B: Environ* 250:313–324
- [2] An X, Yu JC, Wang F, Li C, Li Y (2013) One-pot synthesis of In₂S₃ nanosheets/graphene composites with enhanced visible-light photocatalytic activity. *Appl Catal B: Environ* 129:80–88
- [3] Guo F, Li M, Ren H, Huang X, Hou W, Wang C, Shi W, Lu C (2019) Fabrication of p-n CuBi₂O₄/MoS₂ heterojunction with nanosheets-on-microrods structure for enhanced photocatalytic activity towards tetracycline degradation. *Appl Surf Sci* 491:88–94
- [4] Shi W, Li M, Ren H, Guo F, Huang X, Shi Y, Tang Y (2019) Construction of a 0D/1D composite based on Au nanoparticles/CuBi₂O₄ microrods for efficient visible-light-driven photocatalytic activity. *Beilstein J Nanotechnol* 10:1360–1367
- [5] Shi W, Li M, Huang X, Ren H, Guo F, Yan C (2020) Three-dimensional Z-Scheme Ag₃PO₄/Co₃(PO₄)₂@Ag heterojunction for improved visible-light photocatalytic degradation activity of tetracycline. *J Alloy Compd* 818:152883–152893
- [6] Shi W, Li M, Huang X, Ren H, Guo F, Tang Y, Lu C (2020) Construction of CuBi₂O₄/Bi₂MoO₆ p-n heterojunction with nanosheets-on-microrods structure for improved photocatalytic activity towards broad-spectrum antibiotics degradation. *Chem Eng J* 394:125009–125019
- [7] Mousavi M, Habibi-Yangjeh A, Pouran SR (2017) Review on magnetically separable graphitic carbon nitride-based nanocomposites as promising visible-light-driven photocatalysts. *J Mater Sci: Mater El* 29:1719–1747
- [8] Ri C, Kim S, Ju K, Ryo H, Mun C, Kim U (2018) The synthesis of a Bi₂MoO₆/Bi₄V₂O₁₁ heterojunction photocatalyst with enhanced visible-light-driven photocatalytic activity. *RSC Adv* 8:5433–5440
- [9] Shi W, Ren H, Huang X, Li M, Tang Y, Guo F (2020) Low cost red mud modified graphitic carbon nitride for the removal of organic pollutants in wastewater by the synergistic effect of adsorption and photocatalysis. *Sep Purif Technol* 237:116477–116485
- [10] Guo F, Huang X, Chen Z, Ren H, Li M, Chen L (2020) MoS₂ nanosheets anchored on porous ZnSnO₃ cubes as an efficient visible-light-driven composite photocatalyst for the degradation of tetracycline and mechanism insight. *J Hazard Mater* 390:122158–122170
- [11] Shi W, Shu K, Sun H, Ren H, Li M, Chen F, Guo F (2020) Dual enhancement of capturing photogenerated electrons by loading CoP nanoparticles on N-deficient graphitic carbon nitride for efficient photocatalytic degradation of tetracycline under visible light. *Sep Purif Technol* 246:116930–116939
- [12] Kaspar TC, Schreiber DK, Spurgeon SR, McBriarty ME, Carroll GM, Gamelin DR, Chambers SA (2016) Built-in potential in Fe₂O₃-Cr₂O₃ superlattices for improved photoexcited carrier separation. *Adv Mater* 28:1616–1622

- [13] Lin Y, Zhou S, Sheehan SW, Wang D (2011) Nanonet-based hematite heteronanostructures for efficient solar water splitting. *J Am Chem Soc* 133:2398–2401
- [14] Qu J, Yu Y, Cao C, Song W (2013) α -Fe₂O₃ Nanodisks: layered structure, growth mechanism, and enhanced photocatalytic property. *Chem Eur J* 19:11172–11177
- [15] Warren SC, Voitchovsky K, Dotan H, Leroy CM, Cornuz M, Stellacci F, Hebert C, Rothschild A, Gratzel M (2013) Identifying champion nanostructures for solar water-splitting. *Nat Mater* 12:842–849
- [16] Kang S, Jang J, Pawar RC, Ahn S-H, Lee CS (2018) Low temperature fabrication of Fe₂O₃ nanorod film coated with ultra-thin g-C₃N₄ for a direct z-scheme exerting photocatalytic activities. *RSC Adv* 8:33600–33613
- [17] Wei Y, Han S, Walker DA, Warren SC, Grzybowski BA (2012) Enhanced photocatalytic activity of hybrid Fe₂O₃-Pd nanoparticulate catalysts. *Chem Sci* 3:1090–1094
- [18] Mishra M, Chun D (2015) α -Fe₂O₃ as a photocatalytic material: a review. *Appl Catal A-Gen* 498:126–141
- [19] Singh VK, Patra MK, Manoth M, Gowd GS, Vadera SR, Kumar N (2009) In situ synthesis of graphene oxide and its composites with iron oxide. *New Carbon Mater* 24:147–152
- [20] Arcibarorozco JA, Bandosz TJ (2015) Visible light enhanced removal of a sulfur mustard gas surrogate from a vapor phase on novel hydrous ferric oxide/graphite oxide composites. *J Mater Chem* 3:220–231
- [21] Paulose S, Raghavan R, George BK (2016) Graphite oxide-iron oxide nanocomposites as a new class of catalyst for the thermal decomposition of ammonium perchlorate. *RSC Adv* 6:45977–45985
- [22] Qiu B, Zhu Q, Du M, Fan L, Xing M, Zhang J (2017) Efficient solar light harvesting Cds/Co₉S₈ hollow cubes for Z-scheme photocatalytic water splitting. *Angew Chem Int Ed Engl* 56:2684–2688
- [23] Wang K, Zhang G, Li J, Li Y, Wu X (2017) 0D/2D Z-Scheme heterojunctions of bismuth tantalate quantum dots/ultrathin g-C₃N₄ nanosheets for highly efficient visible light photocatalytic degradation of antibiotics. *ACS Appl Mater Interfaces* 9:43704–43715
- [24] Jia Y, Ma H, Zhang W, Zhu G, Yang W, Son N, Kang M, Liu C (2019) Z-scheme SnFe₂O₄-graphitic carbon nitride: Reusable, magnetic catalysts for enhanced photocatalytic CO₂ reduction. *Chem Eng J* 383:123172–123183
- [25] Jiang Z, Wan W, Li H, Yuan S, Zhao H, Wong PK (2018) A hierarchical Z-scheme alpha-Fe₂O₃/g-C₃N₄ hybrid for enhanced photocatalytic CO₂ reduction. *Adv Mater* 30:1706108–1706117
- [26] Li Y, Liu Y, Hao Y, Wang X, Liu R, Li F (2020) Fabrication of core-shell BiVO₄@Fe₂O₃ heterojunctions for realizing photocatalytic hydrogen evolution via conduction band elevation. *Mater Design* 187:108379–108388
- [27] Liao A, Zhou Y, Xiao L, Zhang C, Wu C, Asiri AM, Xiao M, Zou Z (2018) Direct Z scheme-fashioned photoanode systems consisting of Fe₂O₃ nanorod arrays and underlying thin Sb₂Se₃ layers toward enhanced photoelectrochemical water splitting performance. *Nanoscale* 11:109–114
- [28] Li M, Tang Y, Shi W, Chen F, Shi Y, Gu H (2018) Design of visible-light-response core-shell Fe₂O₃/CuBi₂O₄ heterojunctions with enhanced photocatalytic activity towards the degradation of tetracycline: Z-scheme photocatalytic mechanism insight. *Inorg Chem Front* 5:3148–3154
- [29] Zhang J, Zhang M, Lin L, Wang X (2015) Sol processing of conjugated carbon nitride powders for thin-film fabrication. *Angew Chem* 54:6297–6301
- [30] Xu J, Wang Z, Zhu Y (2017) Enhanced visible-light-driven photocatalytic disinfection performance and organic pollutant degradation activity of porous g-C₃N₄ nanosheets. *ACS Appl Mater Interfaces* 9:27727–27735
- [31] Guo F, Sun H, Cheng L, Shi W (2020) Oxygen-defective ZnO porous nanosheets modified by carbon dots to improve their visible-light photocatalytic activity and gain mechanistic insight. *New J Chem* 44:11215–11223
- [32] Lin Z, Xiao J, Li L, Liu P, Wang C, Yang G (2016) Nanodiamond-embedded p-type copper(I) oxide nanocrystals for broad-spectrum photocatalytic hydrogen evolution. *Adv Energy Mater* 6:1501865–1501875
- [33] Su L-X, Huang Q-Z, Lou Q, Liu Z-Y, Sun J-L, Zhang Z-T, Qin S-R, Li X, Zang J-H, Dong L, Shan C-X (2018) Effective light scattering and charge separation in nanodiamond@g-C₃N₄ for enhanced visible-light hydrogen evolution. *Carbon* 139:164–171
- [34] Isberg J, Hammersberg J, Johansson E, Wikstrom T, Twitchen DJ, Whitehead AJ, Coe SE, Scarsbrook GA (2002) High carrier mobility in single-crystal plasma-deposited diamond. *Science* 297:1670–1672
- [35] Pastrana-Martinez LM, Morales-Torres S, Carabineiro SAC, Buijnsters JG, Faria JL, Figueiredo JL, Silva AMT (2013) Nanodiamond-TiO₂ composites for heterogeneous photocatalysis. *Chem Plus Chem* 78:801–807
- [36] Yu S, Kang M, Chang H, Chen K, Yu YC (2005) Bright fluorescent nanodiamonds: no photobleaching and low cytotoxicity. *J Am Chem Soc* 127:17604–17605
- [37] Han S, Hu L, Liang Z, Wageh S, Alghamdi AA, Chen Y, Fang X (2014) One-Step Hydrothermal Synthesis of 2D Hexagonal Nanoplates of α -Fe₂O₃/Graphene Composites with Enhanced Photocatalytic Activity. *Adv Funct Mater* 24:5719–5727
- [38] Li L, She X, Yi J, Pan L, Xia K, Wei W, Zhu X, Chen Z, Xu H, Li H (2019) Integrating CoOx cocatalyst on hexagonal α -

- Fe₂O₃ for effective photocatalytic oxygen evolution. *Appl Surf Sci* 469:933–940
- [39] Wang L, Zhou G, Tian Y, Yan L, Deng M, Yang B, Kang Z, Sun H (2019) Hydroxyl decorated g-C₃N₄ nanoparticles with narrowed bandgap for high efficient photocatalyst design. *Appl Catal B: Environ* 244:262–271
- [40] She X, Wu J, Xu H, Zhong J, Wang Y, Song Y, Nie K, Liu Y, Yang Y, Rodrigues MF (2017) High Efficiency Photocatalytic Water Splitting Using 2D α -Fe₂O₃/g-C₃N₄ Z-Scheme Catalysts. *Adv Energ Mater* 7:1700025
- [41] Liu C, Fu Y, Xia Y, Zhu C, Hu L, Zhang K, Wu H, Huang H, Liu Y, Xie T, Zhong J, Kang Z (2018) Cascaded photopotential in a carbon dot-hematite system driving overall water splitting under visible light. *Nanoscale* 10:2454–2460
- [42] Sampaio MJ, Pastrana-Martínez LM, Silva AMT, Buijnsters JG, Han C, Silva CG, Carabineiro SAC, Dionysiou DD, Faria JL (2015) Nanodiamond–TiO₂ composites for photocatalytic degradation of microcystin-LA in aqueous solutions under simulated solar light. *RSC Adv* 5:58363–58370
- [43] Shi H, Fan J, Zhao Y, Hu X, Zhang X, Tang Z (2020) Visible light driven CuBi₂O₄/Bi₂MoO₆ pn heterojunction with enhanced photocatalytic inactivation of *E. coli* and mechanism insight. *J Hazard Mater* 381:121006–121017
- [44] Guo F, Wang L, Sun H, Li M, Shi W (2020) High-efficiency photocatalytic water splitting by a N-doped porous g-C₃N₄ nanosheet polymer photocatalyst derived from urea and N, N-dimethylformamide. *Inorg Chem Front* 7:1770–1779
- [45] Guo F, Shi W, Li M, Shi Y, Wen H (2019) 2D/2D Z-scheme heterojunction of CuInS₂/g-C₃N₄ for enhanced visible-light-driven photocatalytic activity towards the degradation of tetracycline. *Sep Purif Technol* 210:608–615
- [46] Guo F, Huang X, Chen Z, Sun H, Shi W (2020) Investigation of visible-light-driven photocatalytic tetracycline degradation via carbon dots modified porous ZnSnO₃ cubes: mechanism and degradation pathway. *Sep Purif Technol* 253:117518–117528
- [47] Guo F, Wang L, Sun H, Li M, Shi W, Lin X (2020) A one-pot sealed ammonia self-etching strategy to synthesis of N-defective g-C₃N₄ for enhanced visible-light photocatalytic hydrogen. *Int J Hydrogen Energ* 45:30521–30532
- [48] Lu CY, Guo F, Yan QZ, Zhang ZJ, Li D, Wang LP, Zhou YH (2019) Hydrothermal synthesis of type II ZnIn₂S₄/BiPO₄ heterojunction photocatalyst with dandelion-like microflower structure for enhanced photocatalytic degradation of tetracycline under simulated solar light. *J Alloy Compd* 811:151976–151986
- [49] Sun H, Guo F, Pan J, Huang W, Wang K, Shi W (2021) One-pot thermal polymerization route to prepare N-deficient modified g-C₃N₄ for the degradation of tetracycline by the synergistic effect of photocatalysis and persulfate-based advanced oxidation process. *Chem Eng J* 406:126844–126856
- [50] Guo F, Li M, Ren H, Huang X, Shu K, Shi W, Lu C (2019) Facile bottom-up preparation of Cl-doped porous g-C₃N₄ nanosheets for enhanced photocatalytic degradation of tetracycline under visible light. *Sep Purif Technol* 228:115770–115777
- [51] Shi W, Yang S, Sun H, Wang J, Lin X, Guo F, Shi J (2020) Carbon dots anchored high-crystalline g-C₃N₄ as a metal-free composite photocatalyst for boosted photocatalytic degradation of tetracycline under visible light. *J Mater Sci* 56:2226–2240. <https://doi.org/10.1007/s10853-020-05436-2>
- [52] Zhu X, Guo F, Pan J, Sun H, Gao L, Deng J, Zhu X, Shi W (2020) Fabrication of visible-light-response face-contact ZnSnO₃@g-C₃N₄ core-shell heterojunction for highly efficient photocatalytic degradation of tetracycline contaminant and mechanism insight. *J Mater Sci* 56:4366–4379. <https://doi.org/10.1007/s10853-020-05542-1>
- [53] Zhu Q, Sun Y, Na F, Wei J, Xu S, Li Y, Guo F (2019) Fabrication of CdS/titanium-oxo-cluster nanocomposites based on a Ti₃₂ framework with enhanced photocatalytic activity for tetracycline hydrochloride degradation under visible light. *Appl Catal B: Environ* 254:541–550
- [54] Cao M, Wang P, Ao Y, Wang C, Hou J, Qian J (2016) Visible light activated photocatalytic degradation of tetracycline by a magnetically separable composite photocatalyst: graphene oxide/magnetite/cerium-doped titania. *J Colloid Interface Sci* 467:129–139
- [55] Yang Y, Zeng Z, Zhang C, Huang D, Zeng G, Xiao R, Lai C, Zhou C, Guo H, Xue W, Cheng M, Wang W, Wang J (2018) Construction of iodine vacancy-rich BiOI/Ag@AgI Z-scheme heterojunction photocatalysts for visible-light-driven tetracycline degradation: Transformation pathways and mechanism insight. *Chem Eng J* 349:808–821
- [56] Niu J, Ding S, Zhang L, Zhao J, Feng C (2013) Visible-light-mediated Sr-Bi₂O₃ photocatalysis of tetracycline: Kinetics, mechanisms and toxicity assessment. *Chemosphere* 93:1–8
- [57] Lu Z, Yu Z, Dong J, Song M, Liu Y, Liu X, Ma Z, Su H, Yan Y, Huo P (2018) Facile microwave synthesis of a Z-scheme imprinted ZnFe₂O₄/Ag/PEDOT with the specific recognition ability towards improving photocatalytic activity and selectivity for tetracycline. *Chem Eng J* 337:228–241

Publisher's Note Springer Nature remains neutral with regard to jurisdictional claims in published maps and institutional affiliations.